Chapter 16
Effect of Process Induced Stresses on Measurement of FRP Strain Energy Release Rates

Brian T. Werner, Stacy M. Nelson, and Timothy M. Briggs

Abstract Fiber reinforced polymer composites are frequently used in hybrid structures where they are co-cured or co-bonded to dissimilar materials. For autoclave cured composites, this interface typically forms at an elevated temperature that can be quite different from the part's service temperature. As a result, matrix shrinkage and CTE mismatch can produce significant residual stresses at this bi-material interface. This study shows that the measured critical strain energy release rate, G_c, can be quite sensitive to the residual stress state of this interface. If designers do not properly account for the effect of these process induced stresses, there is danger of a nonconservative design. Tests including double cantilever beam (DCB) and end notched flexure (ENF) were conducted on a co-cured GFRP-CFRP composite panel across a wide range of temperatures. These results are compared to tests performed on monolithic GFRP and CFRP panels.

Keywords Composites • Fracture • Residual stress • Cohesive zone • Analysis

16.1 Introduction

Fiber reinforced polymer composite structures are well suited for the tailoring of material properties. Options available to the designer include various fibers, matrices, orientations, and fabric weaves. Often the most efficient structure, both economically and structurally, combines glass fiber reinforced polymer (GFRP) with carbon fiber reinforced polymer (CFRP) into a hybrid structure. While the same matrix may be used, the fibers themselves have greatly different properties. In this study, the focus is placed on both stiffness and coefficient of thermal expansion. Due to these differences, significant residual stresses can develop either when cured at an elevated temperature, such as in an autoclave, or when the structure's service temperature differs from the material's stress free temperature.

Over the past few years, the cohesive zone element and associated traction-separation law have gained prominence when designers employ a fracture based failure criterion for delaminations [1–4]. As long as linear elastic fracture mechanics holds (LEFM), the most important parameter in the traction-separation law is the strain energy release rate, G. Determining the strain energy release rate, G, for a monolithic fiber reinforced polymer is relatively straightforward and follows a standard experimental procedure. However, once significant residual stresses are present along the interface in question, the coupled effect of residual stresses and fracture toughness can produce uncertainty [5, 6]. If an apparent toughening due to the presence of residual stresses is modeled as a higher strain energy release rate, the condition for a nonconservative design arises which can lead to unexpected failure.

By investigating the effect of residual stress in a hybrid specimen across a wide temperature range, the ultimate goal is to decouple the question of the residual stress state and applied loading to develop a more robust cohesive zone or localization element. Perhaps designers can take advantage of an apparent toughening due to residual stress to develop more efficient structures.

All of the testing was performed at three temperatures: subambient (−54 °C), room temperature (+20 °C), and elevated (+71 °C). While all of the testing remained within the glassy regime for the epoxy matrix, the wide temperature range produced significantly different levels of residual stress at the interlaminar interface of interest.

B.T. Werner (✉) • S.M. Nelson • T.M. Briggs
Sandia National Laboratories, 7011 East Avenue, Livermore, CA 94550, USA
e-mail: btwerne@sandia.gov

P.R. Thakre et al. (eds.), *Mechanics of Composite and Multi-functional Materials, Volume 6*,
Conference Proceedings of the Society for Experimental Mechanics Series, DOI 10.1007/978-3-319-63408-1_16

16.2 Material

Three panel types were fabricated from two materials, a carbon/epoxy (CFRP) 8-harness satin weave fabric prepreg and a glass/epoxy (GFRP) 8-harness satin weave prepreg. The panels consisted of GFRP bonded to GFRP, $[(0/90)_{7s}]_s$, CFRP bonded to CFRP, $[(0/90)_{4s}]_s$, and GFRP bonded to CFRP, $[(0/90)_{10s}{}^{glass}/(0/90)_{5s}{}^{carbon}]$. All three laminates were laid up to produce two symmetric beams with an equivalent bending stiffness and a Teflon strip was embedded along one edge at the warp-to-warp interface between the two beams to produce a precrack. The prepreg layup was co-cured using a standard cure schedule that has been developed for this material [7]. This produced a material with V_f of 0.60 and E_{11} of 30 GPa for the GFRP and 60 GPa for the CFRP.

The panels were cut into specimens approximately 25 mm wide and 200 mm long with the Teflon precrack at one end using a water cooled diamond tile saw. The initial length of the precrack was approximately 38 mm long. The total thicknesses of each specimen were 6.82 mm for the GFRP/GFRP and 7.68 for the CFRP/CFRP bulk material specimens, and 8.75 mm for the GFRP/CFRP hybrid specimens. For the DCB and asymmetric-DCB (ADCB) specimens, hinges were bonded to each face of the precracked end using a secondary bond. The surfaces of both the specimen and the hinge were abraded lightly with coarse grit sandpaper to improve adhesion and two different epoxies were used. For the room temperature and subambient testing a high strength epoxy (Hysol 9430) was used but for the elevated temperature testing a high temperature structural adhesive had to be employed (Hysol 9394).

16.3 Experimental Procedure

The experiments were carried out using an Instron 5989 electromechanical load frame using 2kN and 10kN load cells and an environmental chamber. The three temperatures investigated were +71 °C, +25 °C, and −54 °C. These temperatures provide a wide range of ΔT's and, with that, significantly different residual stress states in the bi-material specimens. A type K thermocouple was attached to the surface of the specimen to monitor its temperature. Each specimen was allowed time for the temperature to equilibrate before testing was initiated. Prior to starting the test, the specimen was held in load control at a low force to allow the fixturing to expand or contract with the temperature without applying significant load to the specimen. The load cell was also held outside of the environmental chamber with a fan blowing on it to ensure that there was minimal thermal drift in the load reading.

16.3.1 DCB Testing

DCB tests were performed in accordance with ASTM standard D5528–13 [8]. Initial tests used a laser extensometer to track the crack opening displacement but after comparison with the stroke measurement, little error was found due to frame compliance at the low loads applied. Each specimen was tested at a constant displacement rate of 1 mm/min (Fig. 16.1).

Crack lengths and the applied energy release rate were calculated using elastic beam theory to back out the current crack length from the measured load-displacement data. For the bulk material the equations used were:

$$a = \left[\frac{\delta E b h^3}{8P}\right]^{\frac{1}{3}} \tag{16.1}$$

$$G_{app} = \frac{12P^2a^2}{Ebh^3} \tag{16.2}$$

For the asymmetric DCB, Brown et al., derived the beam theory solution for the crack length, a, and applied energy release rate at the crack tip, G_{app} [9]:

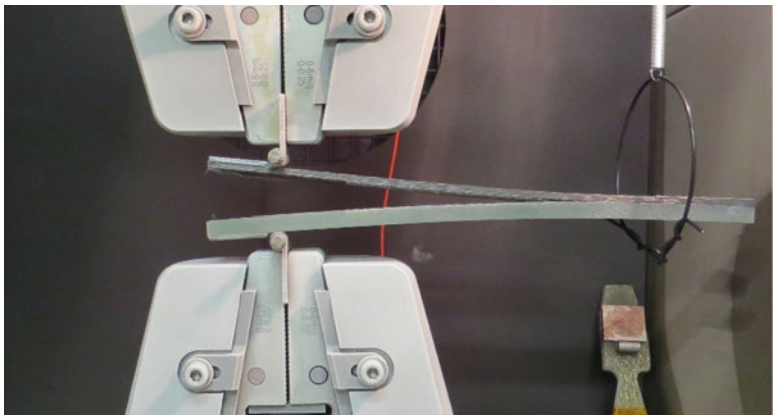

Fig. 16.1 DCB test setup

$$a = \left[\frac{\delta b}{16P}\left(E_1 h_1^3 + E_2 h_2^3\right)\right]^{\frac{1}{3}} \tag{16.3}$$

$$G_{app} = \left[\frac{27\delta P^4}{2b^4}\left(\frac{1}{E_1 h_1^3} + \frac{1}{E_2 h_2^3}\right)\right]^{\frac{1}{3}} \tag{16.4}$$

where P = load
b = width of DCB
d = crack opening displacement
E_i = Young's modulus of material *i*
h_i = thickness of laminate *i*

16.3.2 ENF Testing

For fabric composites there is no ASTM standard for the determination of Mode II energy release rate. For unidirectional composites it is ASTM D7905/D7905M-14 [10] which is the ENF specimen (Fig. 16.2), however when switching to a fabric composite there are additional complications that can make accurate determinations of energy release rate more difficult. The main problem is friction in the pre-cracked section of the specimen. As the beam is loaded, the cracked faces rub against one another which dissipates energy and can lead to error by increasing the apparent energy release rate. This is further complicated by the fact that the ENF test is unstable for initial crack lengths shorter than 0.69 L where the specimen has a total span of 2 L. With such a large length, the precracked area that is susceptible to friction is quite large. Some investigators have balanced this by performing the test with shorter crack lengths which leads to unstable crack growth [11]. This may also produce experimental error as the energy dissipation calculated by the load displacement curve cannot account for the true energy released (Fig. 16.3).

The load displacement curve from the experiment follows the solid line in Fig. 16.3, but the actual energy released follows the dashed line. The experimental error is equivalent to the size of the lobed region to the left of the rapid crack growth line. Some researchers prefer the End Loaded Split (ELS) test that uses a cantilever beam approach with the precracked section at the free end. By pulling up on the free end from both the top and bottom adherend with the same load, the problem of friction is solved. The test is also inherently stable. However, for this study the ENF test was pursued to compare with legacy data. An issue also arises from the overhang on the support roller on the precracked end of the ENF specimen. Despite the beam being unloaded outside of the support rollers, energy may still be dissipated due to friction from contact. For all of these reasons an initial study was performed to determine the ideal test geometry to produce consistent results. Parameters such as temperature (20 °C) and orientation (GFRP up) were held constant while initial crack length and span were varied. With a span of 2 L set at 102 mm, 127 mm, or 152 mm, the initial crack length was varied from 0.3 L, 0.5 L, and 0.69 L. Testing of a minimum of three specimens under each condition was performed to provide some statistical value. Overhang was not considered during this round of testing, but was measured to determine its effect after the tests (Fig. 16.4).

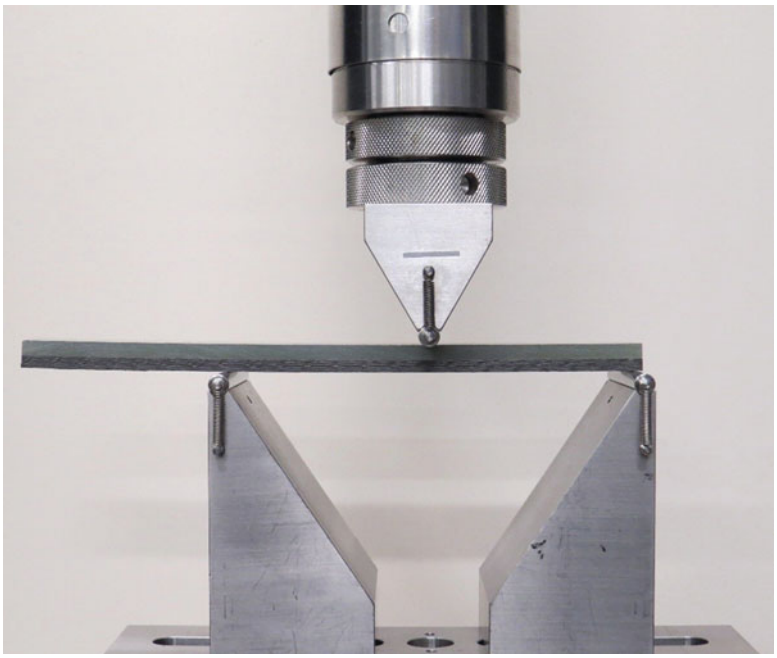

Fig. 16.2 ENF test setup

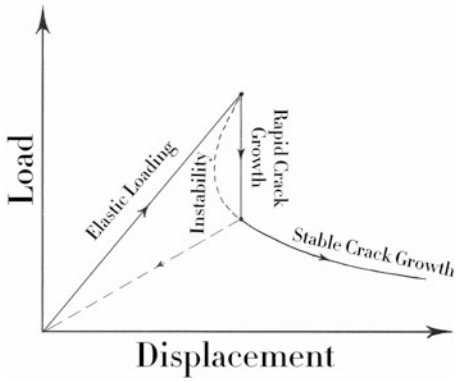

Fig. 16.3 Instability of ENF test [12]

Where the test had similar overhang lengths, no conclusions could be drawn to its effect. However, for tests that had varying overhangs for the same test condition, the effect is quite clear qualitatively. The longer the overhang protrudes from the support roller on the specimen's cracked end, the greater the frictional losses and the more the energy release rate is overestimated. All of the dashed lines in Fig. 16.4 trace back to approximately 1100–1200 J/m^2.

Each test was performed in the Instron 5989 electromechanical load frame. The displacement was measured using a laser extensometer to remove the effect of system compliance. The specimens were loaded at a displacement rate of 1 mm/min and when the crack extended to approximately the midspan they were unloaded at the same rate. The total energy dissipated was obtained by integrating the load displacement curve. The displacement may not have unloaded to 0 as the curvature of the beam changed once residual stress was released. To measure the crack area, the transparency of the GFRP was taken advantage of. The initial crack area could be easily seen and measured before and after testing. A reference line was drawn across the width of the specimen in the precracked region. A Keyence VHX-5000 digital microscope on 30× zoom and image stitching was then used to measure the crack area in the software. This microscope was calibrated using a NIST traceable calibration scale to produce accurate measurements. This area was then compared to the area post-test to determine the total crack amount of crack growth (Fig. 16.5). The quotient of the two values, energy dissipation and crack growth area were then used to determine energy release rate, G.

For the unstable crack growth specimens like that shown in Fig. 16.5, there is a steep load drop once the crack extends. In the stable crack growth specimens the load drops more gradually until it reaches the load roller in which case it begins to pick

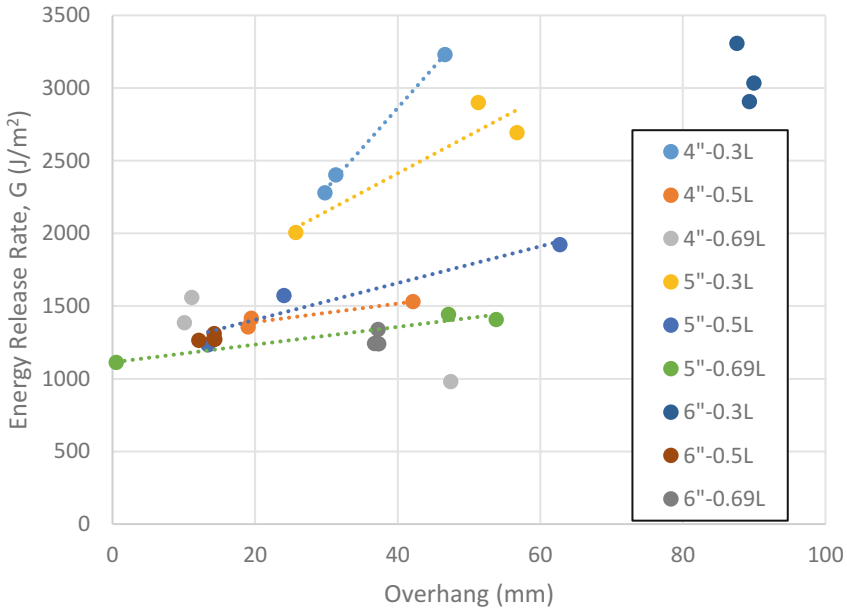

Fig. 16.4 Overhang effect on energy release rate

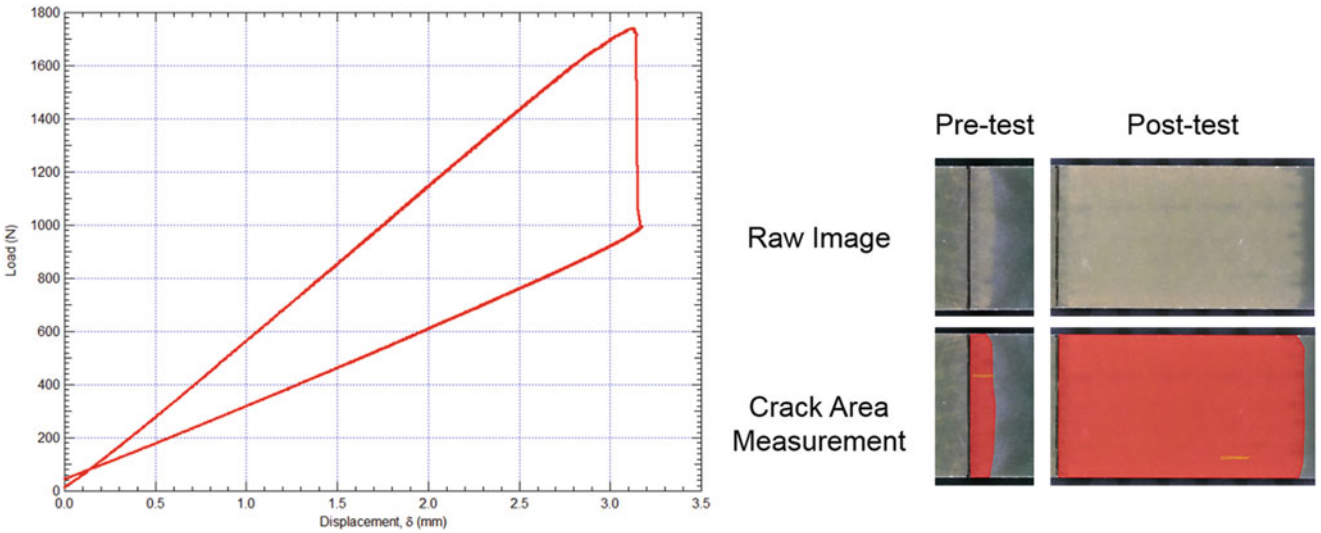

Fig. 16.5 Load-displacement curve of a typical ENF test (*left*) and crack area measurement images (*right*)

back up again. It is at that minimum load at which the specimen is unloaded. The results of the test geometry study are shown in Table 16.1 below.

The short crack length of 0.3 L produced the most energy dissipation and was so unstable the crack tended to grow beyond the load roller. It was also more likely to produce what appeared to be multiple cracks in interlaminar regions away from the interface of interest. The other two crack lengths produced similar results while the 0.5 L crack length was more consistent than the 0.69 L crack length due to its lower coefficient of variation. Either would work fine for a study though. The 0.5 L crack length was chosen for its repeatability, lower friction, larger area of crack growth, and less of an impact to the calculated energy release rate from the variations in the stress field due to Hertzian contact as the crack approached the load roller. The largest span was also chosen because it results in lower applied loads, a larger precracked area to carry those loads, and thus lower frictional losses. A plot tabulating the results in Table 16.1 is shown in Fig. 16.6.

For all of the following testing at the various temperatures and orientations, the span had a length of 152 mm and the specimen had a precrack length of 37 mm. While a Teflon strip was used to produce the precrack during the cure, the crack was manually extended with the use of a razor blade wedging open the precracked side to form a sharp crack tip for the testing. For the bulk material testing, the tests were limited to the GFRP-GFRP specimens as the crack surfaces could be

Table 16.1 Energy release rates for various test geometries

Span (2 L)	Crack length	G Avg (J/m^2)	COV (%)
102 mm	0.3 L	2636	16.1
	0.5 L	1434	5.0
	0.69 L	1308	18.6
127 mm	0.3 L	2532	15.1
	0.5 L	1575	8.8
	0.69 L	1319	25.2
152 mm	0.3 L	3082	5.4
	0.5 L	1282	1.6
	0.69 L	1273	3.7

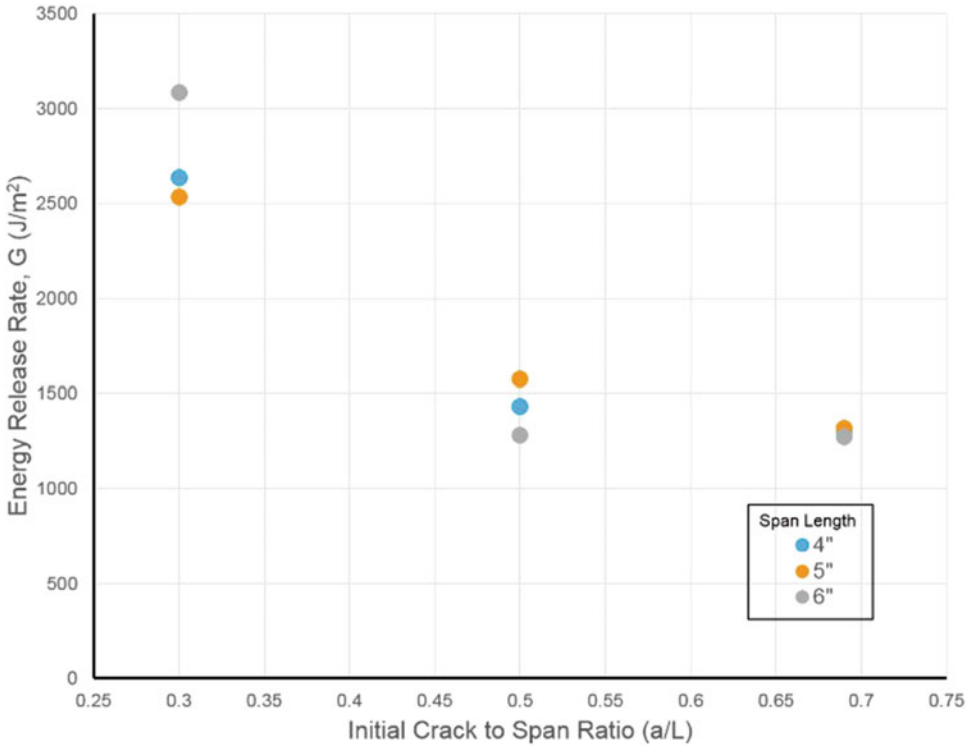

Fig. 16.6 Calculated energy release rates from varying initial crack lengths and spans

inspected visually. The bi-material specimens were tested at all three temperatures in two orientations, with the load roller pressing on the CFRP and with the load roller pressing on the GFRP.

16.4 Results

16.4.1 DCB Results

The bulk material GFRP-GFRP and CFRP-CFRP specimens showed no temperature dependence on the energy release rate as shown in Fig. 16.7. The CFRP-CFRP specimens do display a slight rising resistance curve at the ambient and elevated temperatures. This may appear to be evidence of fiber bridging, like in unidirectional composites, but this phenomenon was not observed during the testing. The GFRP has a critical energy release rate of approximately 280 J/m^2 while the CFRP varied from 280–320 J/m^2. The similarity is not surprising as they both contain the same matrix. The GFRP may be slightly less tough as the fracture surface appeared to fail at the fiber-resin interface as there was dry fiber on one of the fractured

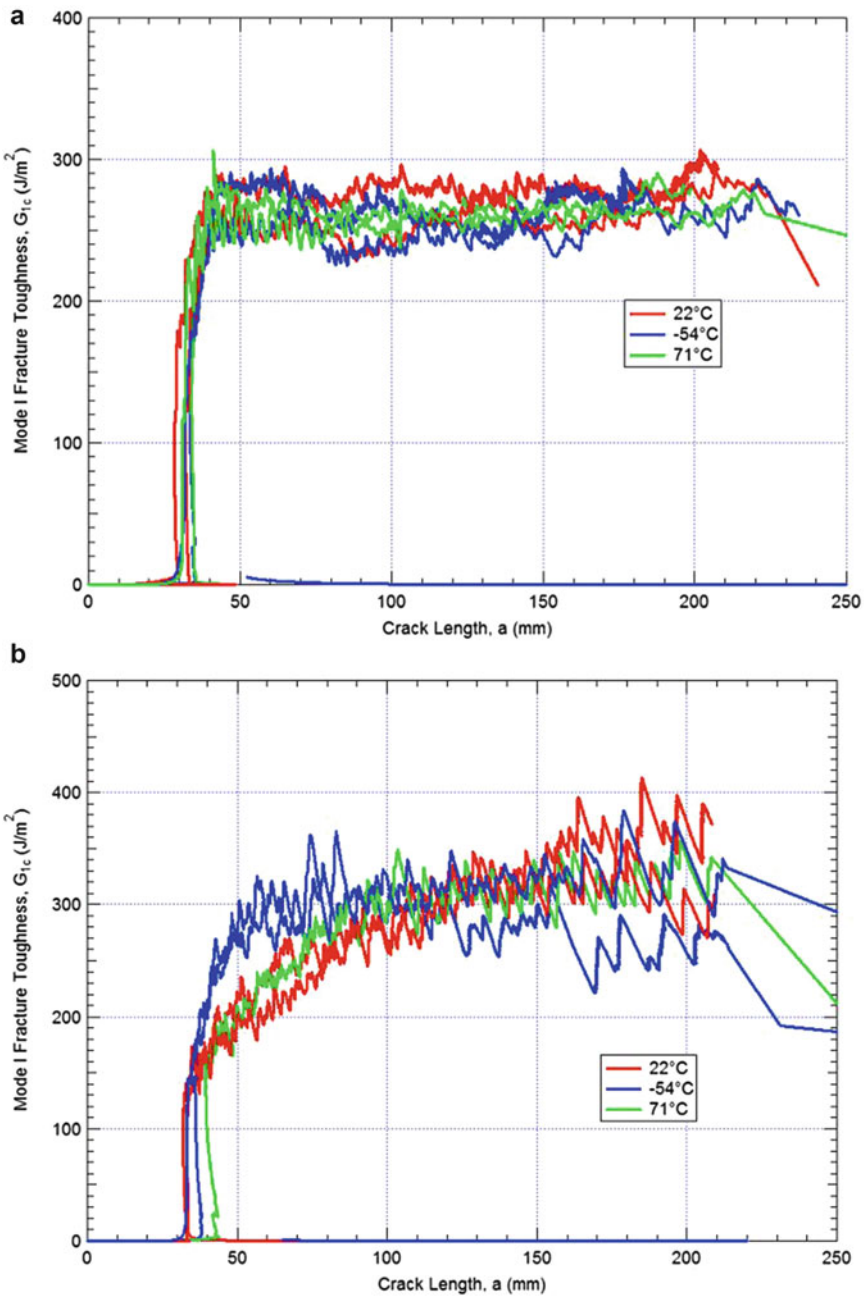

Fig. 16.7 Energy release rate vs crack length for (**a**) GFRP/GFRP and (**b**) CFRP/CFRP laminates

surfaces. The CFRP also presented more of a skip start behavior but this was likely due to larger resin rich regions since it has a coarser weave than the GFRP.

Unlike the bulk material DCB tests, the ADCB shows a significant temperature dependence (Fig. 16.8). As the temperature drops, the ΔT increases which leads to higher residual stresses at the bi-material interface. Since higher residual stresses are correlated with higher apparent strain energy release rate it is assumed that there is a complex stress state at the crack tip. With the help of computational methods, the stress fields at the crack tip can be investigated further to determine whether it is simply the residual stresses producing a stress state that is counter to the applied loading or perhaps the in-plane shear stresses along the interface are producing mixed-mode behavior. It is also worth pointing out that in the bulk material DCB tests, the critical energy release rate for the GFRP was slightly under 300 J/m^2 and the CFRP is between 250 and 350 J/m^2. However, in the ADCB tests, the elevated temperature, least tough experiment showed a critical energy release rate of around 400 J/m^2, higher than that of any of the bulk material tests. This further suggests that the small amount of residual stress even at elevated temperature is beneficial to the crack propagation resistance.

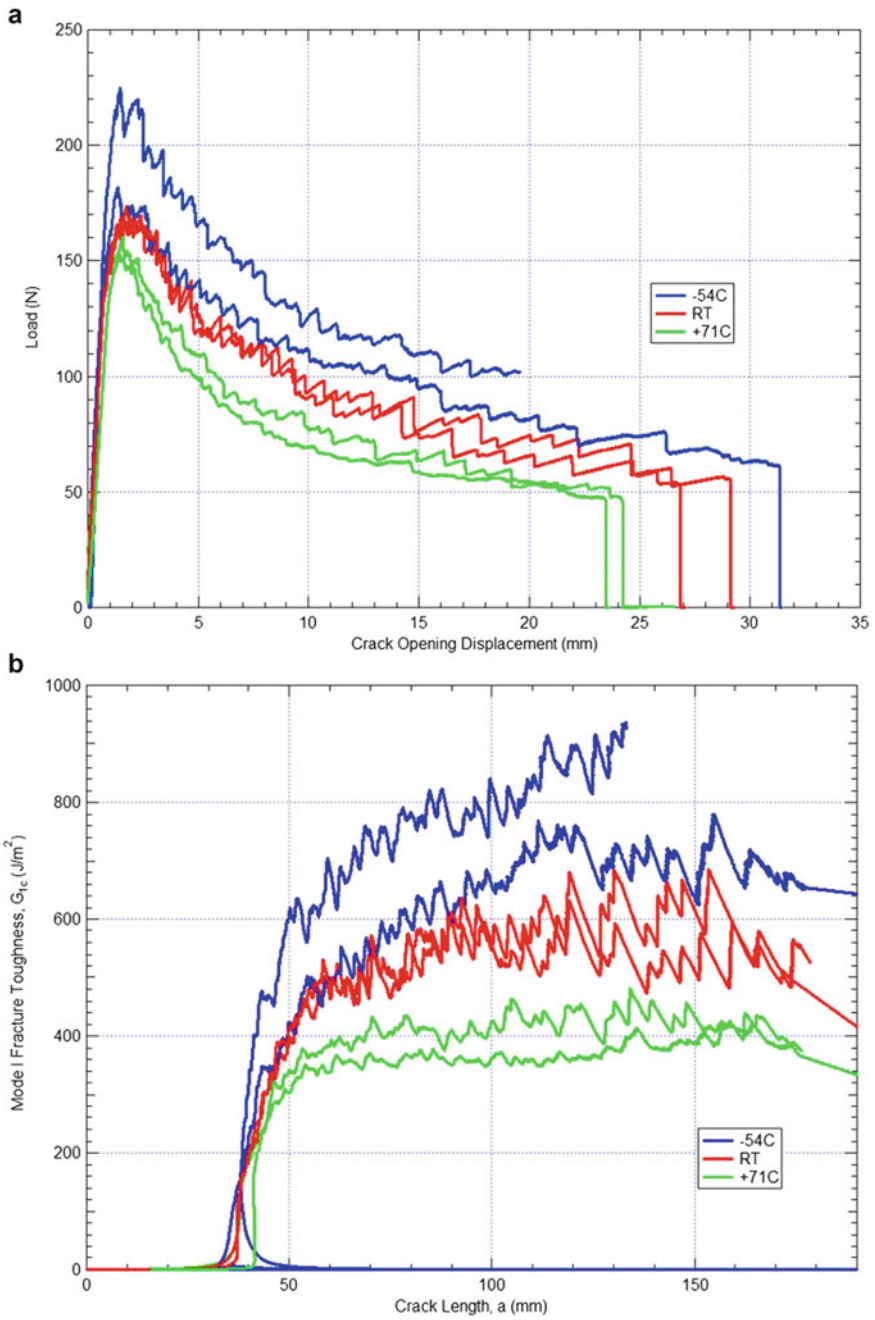

Fig. 16.8 (**a**) Load-displacement and (**b**) energy release rate vs crack length for ADCB laminate

When investigating the fracture surfaces, a change in the mode of crack propagation is seen (Fig. 16.9). At the subambient temperature, all of the resin is pulled off of the CFRP, showing dry fibers. At the elevated temperature, all of the resin is pulled off of the GFRP, showing dry fibers. At room temperature, the failure appears to be more cohesive within the resin layer.

Without accounting for the effect of residual stresses, the bi-material interface can appear significantly tougher. This can lead to a structural design that is nonconservative.

16.4.2 ENF Results

The testing was limited to GFRP-GFRP for the bulk material as ultrasonic inspection would be needed to determine initial and final crack areas. This work is planned and ongoing. Typical load displacement curves for the hybrid specimens can be seen in Fig. 16.10.

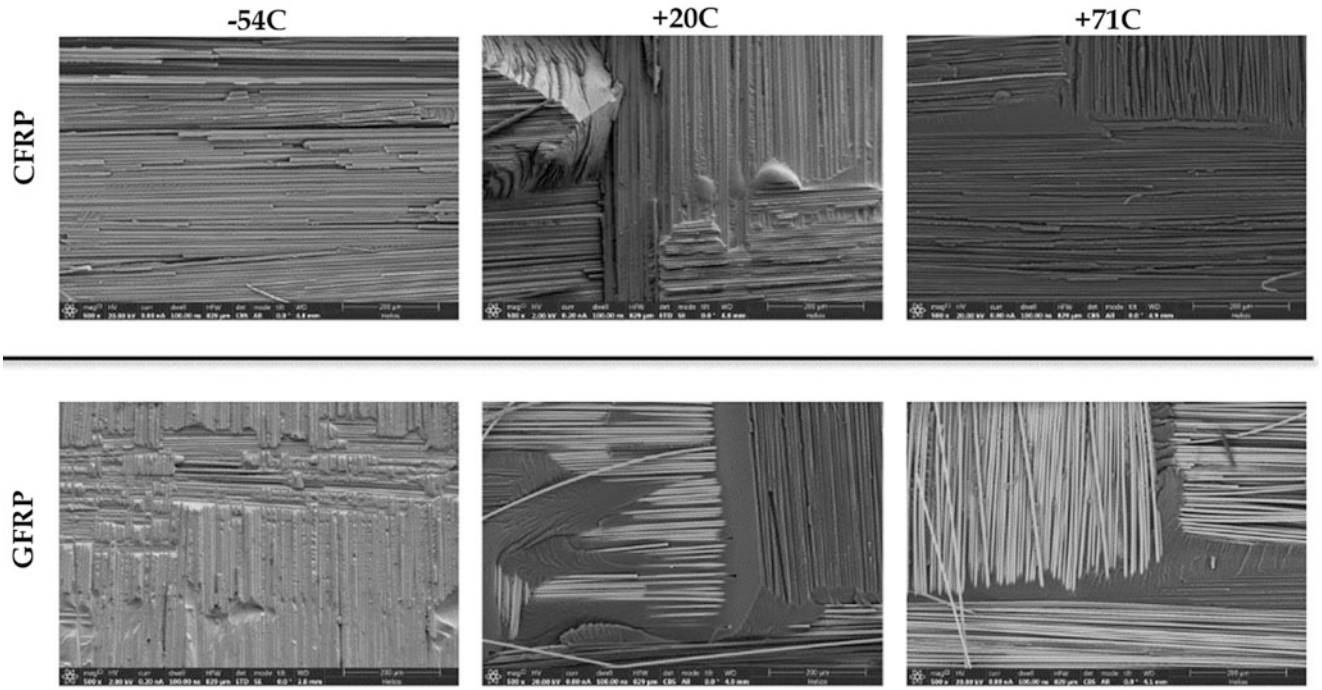

Fig. 16.9 SEM images of the fracture surfaces in the bi-material specimen at each temperature (500× magnification)

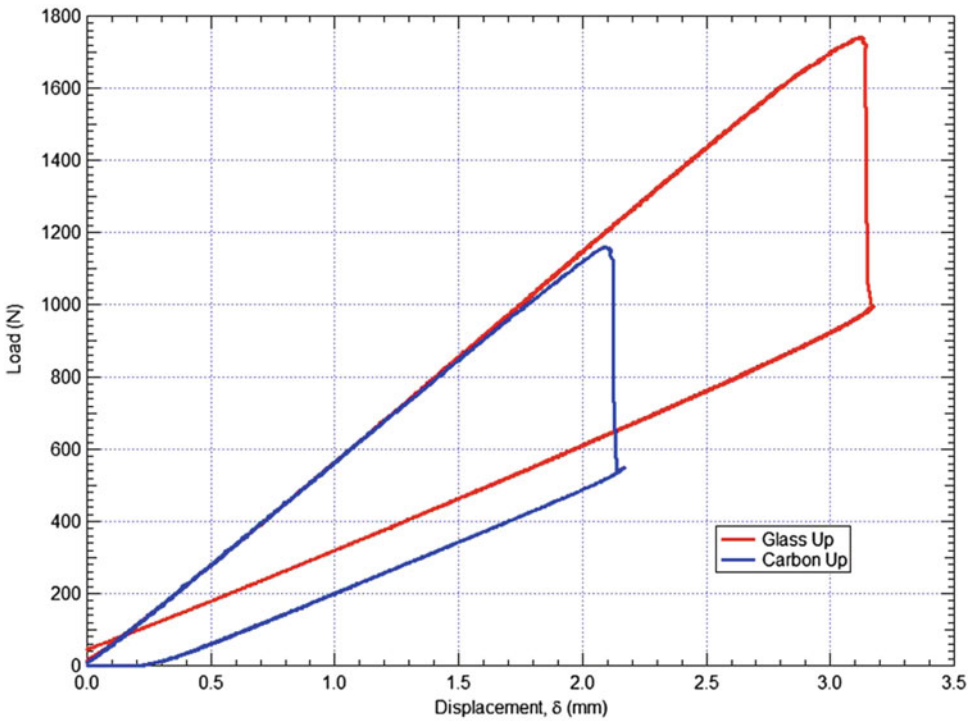

Fig. 16.10 Load-displacement curves for hybrid ENF specimens

Table 16.2 Strain energy release rate results for ENF testing

Specimen type	Temperature	Face up	G_{Avg} (J/m^2)	COV (%)
GFRP	71 °C	N/A	1230	2.1
	20 °C		1172	0.6
	−54 °C		1856	5.6
Bi-material	71 °C	Carbon	869	5.7
		Glass	1224	5.6
	20 °C	Carbon	733	2.9
		Glass	1281	1.6
	−54 °C	Carbon	882	4.9
		Glass	1889	2.1

The orientation of the specimen has a strong impact on the specimen's response. This is most likely due to significant shear at the bi-material interface. In one orientation, CFRP facing up, this residual shear is acting in the same direction as the applied bending load so they work constructively to extend the crack. However, when the GFRP is facing up, the applied bending load must overcome the residual stress before the crack is extended. This trend is further pronounced as the ΔT increases. Such a response is not seen in the bulk material GFRP specimens. A table listing the results from this portion of the study is shown below (Table 16.2).

For each material under each load case, the subambient testing produced strain energy release rates approximately 50% higher than what the trend would suggest from the elevated and ambient testing. This is most likely due to additional crack surfaces being formed in adjacent ply interfaces due to crack jumping. Ultrasonic inspection is currently being performed on these specimens to correct for the enhanced strain energy release rate. Another possible solution is to perform these tests with a longer initial crack length as in the test geometry study, the more unstable crack growth also produced multiple cracks.

16.5 Simulation Methodology

As presented in the previous section, the formation of residual stresses improved the measured fracture toughness only in the carbon-glass DCB specimens. This implies that the observed trend is related to the formation of residual stresses, rather than some temperature dependency in the material properties. Therefore, computational methods were developed to simulate the effect of residual stress formation within the carbon-glass DCB specimens to better understand the bondline's stress evolution, the stress fields around the crack tip, and potential drivers for the increasing fracture toughness.

16.5.1 Analysis Software

All simulations were completed using Sandia National Laboratories' Sierra Solid Mechanics code Adagio. Adagio is a Lagrangian, three-dimensional code for the finite element analysis of solid structures and is suitable for implicit, quasi-static analyses. Also, Sierra Adagio can make use of a multi-level solver, the solution core of which is a nonlinear, conjugate gradient algorithm that can iteratively find a solution that is within some user-defined tolerance of equilibrium. Use of the multi-level solver within Adagio aids in the solution of problems containing such challenging aspects as contact, materials with non-linear responses or extreme differences in stiffness, and material failure with element death [13].

16.5.2 Element Formulation

The modeled components were simulated with eight-noded hexahedral elements. While Sierra Adagio's default element formulation utilizes a computationally efficient, single point integration rule, avoidance of potential numerical inaccuracies common to an under-integrated element (e.g., hourglass modes) was necessary as a failure process would be modeled in these simulations. Therefore, Sierra Adagio's selective deviatoric element formulation was instead applied. This element

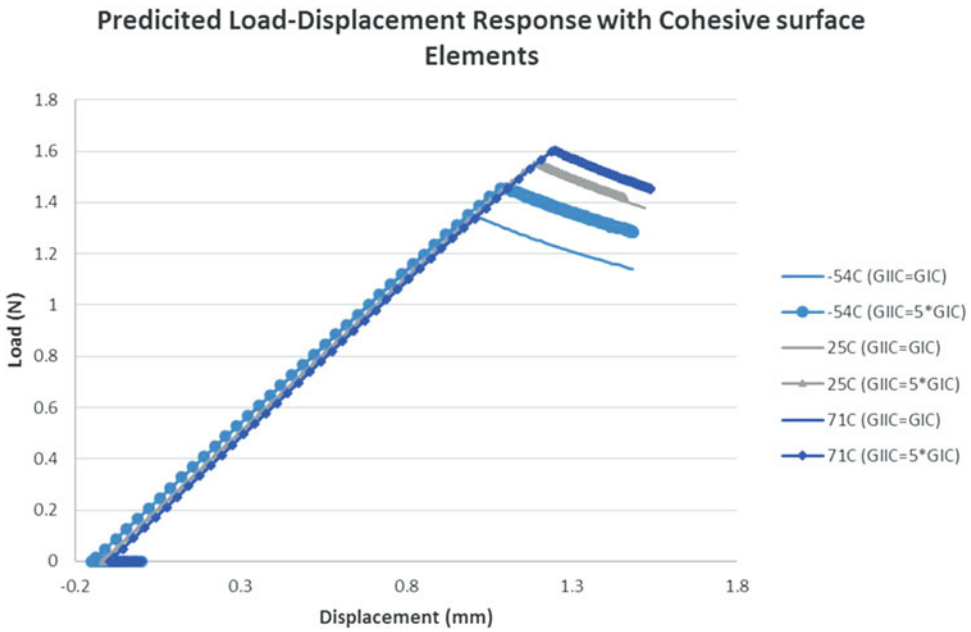

Fig. 16.11 Sample load-displacement response of DCB experiment predicted with cohesive zone methods

type is fully integrated with respect to the deviatoric stress response and under-integrated with respect to the hydrostatic pressure response [13].

Also, note that while most investigations regarding the simulation of crack growth in fiber reinforced polymer composites make use of cohesive surface elements to extrapolate the complexity of a bonded interface to a surface element, the bondline in the current study was modeled with the same hexahedral elements as the composite adherends. As it has been postulated that the fracture toughness increase may in part be due to contraction of the bondline material, it was necessary to model the adhesive layer with an element capable of thermal contractions and surface elements are not able to exhibit such behaviors. To verify the assumption that the correct experimental trend could not be modeled using a traditional cohesive zone modeling approach, several preliminary simulations were completed utilizing a surface element in conjunction with cohesive models with and without a mixed-mode resistance. The results of these preliminary simulations were not able to match the experimentally observed trend. Rather the cohesive zone model results imply that increasing amounts of residual stresses should decrease the experimentally measured fracture toughness and failure load. Figure 16.11 describes the typical results from these cohesive zone model simulations.

While the results shown in the above plot do not match the experimentally observed trend, they do indicate the potential importance of mode mixity. Specifically, as shown in the plot, increasing the mode II fracture toughness effectively increases the predicted peak loads for the 25 °C and −54 °C simulations. Alternatively, increasing the mode II behavior had no noticeable effect on the 71 °C predictions. This observation may indicate that large out-of-plane shear strains, that must be overcome prior to fracture, form along the bondline and increase progressively with greater excursions from the stress-free temperature.

16.5.3 Material Models

The individual components of the simulated DCB geometry were modeled with three materials: the adherends were made of either the carbon or glass composite and the bondline was modeled as neat epoxy. As no yielding or failure was anticipated in either the carbon or glass adherends, these materials were simulated with Sierra Adagio's elastic-orthotropic model. This model requires the definition of the regular nine elastic constants as well as glassy and rubbery coefficients of thermal expansion in each of the materials' orthotropic directions [13]. These properties, which were determined either through experimental testing or micromechanical modeling, are listed in Table 16.3 for the glass and carbon composite materials.

Table 16.3 Material properties used to define the carbon and glass composite materials

	CFRP	GFRP
E_{11} (GPa)	63.9	24.8
E_{22} (GPa)	62.7	23.1
E_{33} (GPa)	8.6	9.7
G_{12} (GPa)	3.44	3.4
G_{13} (GPa)	3.27	2.9
G_{23} (GPa)	3.25	2.9
ν_{12}	0.048	0.13
ν_{13}	0.408	0.36
ν_{23}	0.408	0.36
CTE_{11} (rubbery) (ppm/°C)	1.14	8.31
CTE_{22} (rubbery) (ppm/°C)	1.36	9.88
CTE_{33} (rubbery) (ppm/°C)	282.9	343.5
CTE_{11} (glassy) (ppm/°C)	3.41	17.3
CTE_{22} (glassy) (ppm/°C)	3.42	17.9
CTE_{33} (glassy) (ppm/°C)	72	65.6
T_g (°C)	122.7	104.5
Stress-Free Temperature (°C)	140	140

Table 16.4 Material properties used to define the bondline adhesive

Young's Modulus (GPa)	4.0
Poisson's ratio	0.35
CTE (ppm/°C)	45.0

Next, according to recommendations from literature, the bondline epoxy material was modeled with Sierra Adagio's elastic model, which requires the definition of only the material's Young's modulus, Poisson's ratio, and coefficient of thermal expansion [13]. These material parameters, which were taken from literature, are listed below in Table 16.4 [14–16].

Lastly, to facilitate crack growth within the modeled DCB specimen, it was necessary to define a criterion for element death within the bondline. For simplicity, and according to literature, a maximum strain failure theory was defined and executed for the previously described epoxy material. With this approach, a maximum tensile strain was defined within the adhesive layer, and if this value was exceeded within an element, the offending element was deleted. The maximum failure strain was defined as 2.0% [14]. Note that this process of element deletion was implemented in order to capture both thermal contraction and crack growth within the bondline in a single simulation. However, since finite element methods incorporating element death and deletion are seldom mesh convergent, the methods currently presented in this study cannot be used to make quantitative predictions regarding the material's failure behaviors. Instead the qualitative observations from these current simulations can help prioritize the physical phenomena that should be accounted for during the future development of a cohesive or localization material model suitable for use with a surface element, upon which mesh convergence is generally readily found.

16.5.4 Model Geometry

The simulations were completed with three-dimensional geometries and meshes created using Cubit, which is a robust software toolkit capable of creating both two- and three-dimensional geometries and meshes. As described in the previous sections, since contractions within the bondline were of interest, the adhesive layer was modeled with solid elements. However, as the bondline had an average measured thickness of 0.1 mm and the carbon and glass adherends had thicknesses of 4.9 mm and 3.9 mm, respectively, geometry simplifications were necessary. In order to achieve a resolved stress state within the bondline, the adhesive layer required high quality, refined elements. Therefore, to maintain a reasonable computational cost, a plane-strain model was implemented along with a truncated specimen length. Specifically, while the full 38 mm pre-crack length was modeled, the specimen's simulated bonded length was only 15 mm. This simplification was deemed appropriate, as the experimentally measured fracture toughness was observed to rise to a nearly constant value after the crack grew approximately 10–12 mm (Fig. 16.8). Figure 16.12 shows the modeled DCB geometry without meshlines.

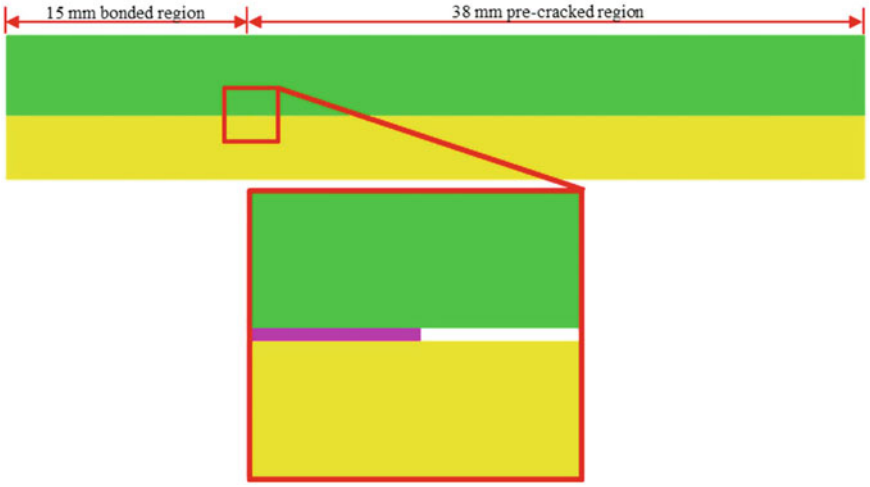

Fig. 16.12 Representative geometry of four-point flexure simulations

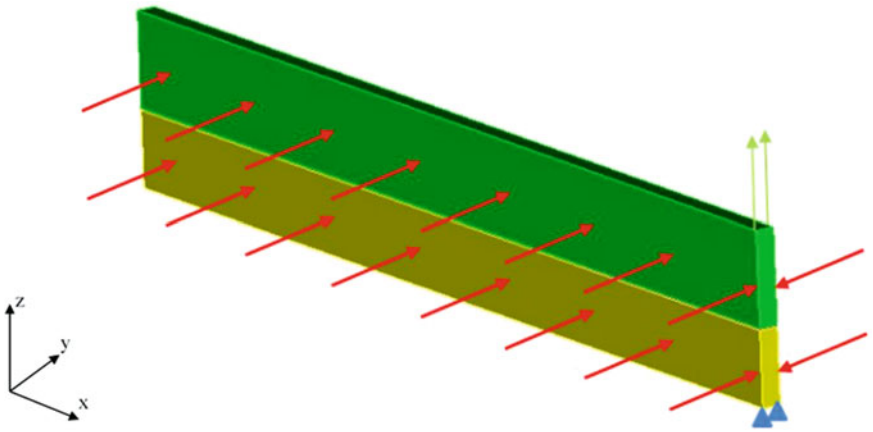

Fig. 16.13 Description of the DCB specimen's applied boundary conditions

Also, note that Sierra Adagio does not include a plane-strain element. Therefore, in order to approximate the plane-strain condition, the geometry shown in Fig. 16.12 was modeled with a depth of only 1 mm and appropriate boundary conditions were applied along the side surfaces of the simulated specimens. These approximations are discussed further in the following section.

16.5.5 Boundary Conditions

Boundary conditions were applied to the DCB experiment simulations to approximate the plane-strain conditions as well as to emulate the formation of the thermal residual stresses and the application of the tensile, mode I loading. First, to approximate the plane-strain boundary conditions, the side surfaces of the specimen were translationally fixed in the depth, or y, direction, as shown by the red arrows in Fig. 16.13. Next, to model the formation of the thermal residual stresses before the application of the mode I loading, the process described in [16] was applied. Specifically, the DCB simulations were initiated will all components at a constant and uniform temperature equal to the experimentally measured stress-free temperature. Then, the modeled specimens were isothermally cooled to the appropriate testing temperature (71 °C, ambient, or −54 °C); and, since the material definitions for the composite and epoxy materials included the appropriate CTE values, residual stresses were formed due to thermal contractions within the bondline and adherends. Lastly, boundary conditions were defined to mimic the associated experimental loading after the simulated cooling process. In the DCB simulation, the bottom-front edge in the pre-cracked region was translationally fixed in the x and z directions (as shown by the blue triangles in Fig. 16.13), while the top-front edge was translationally fixed in the x direction with an applied velocity condition applied in the vertical, or z, direction (as shown by the green arrows in Fig. 16.13). For the ENF simulation, similar boundary

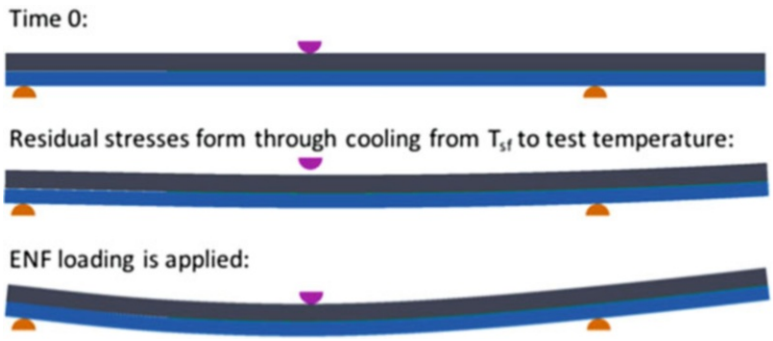

Fig. 16.14 Boundary conditions for the ENF simulations

conditions were applied on the x-z face of the specimen but the two support rollers were fixed in the z direction and the loading was applied by displacing the loading roller in the z direction (Fig. 16.14).

For all of the simulations performed in this study a mesh convergence study was performed in accordance with previous work [18]. The resulting mesh in the DCB simulations was very fine with element lengths of 0.04167 mm which produced discretization errors less than 0.05% when compared to the exact solution obtained through Richardson's Extrapolation at 1 mm of displacement. The ENF simulations used a coarser mesh but the results still yielded errors less than 2% at 1.5 mm of displacement. Note that the mesh convergence study demonstrates verification only prior to the threshold of element deletion, since the critical strain criterion will be met progressively sooner as the element size is made progressively smaller due to the singularity at the crack tip.

16.6 Simulation Results

The computational methods described in the previous sections were developed to aid in understanding the stress evolution within the adhesive layer as well as the potential drivers for the experimentally observed fracture toughness increase. As it has been hypothesized that the measured trends are due to the residual stresses that form as a result of the CTE differential between the composite adherends, contraction within the epoxy bondline, or a combination of these two phenomena, two types of simulations were completed. This first simulation measured the effect of just the residual stresses formed between the carbon and glass composites, while ignoring contractions within the bondline, and the second simulation included the effect of the bondline contractions.

16.6.1 DCB Simulations Without Bondline Contraction

With the modeling approach described in the previous sections and the converged mesh, simulations were first completed to determine the effect of the CTE differential between the carbon and glass adherends on the predicted load-displacement response. Specifically, the temperature boundary condition, described earlier, was applied only to the composite components of the model. The adhesive layer was excluded from the thermal excursion. Figure 16.15 shows the load-displacement response predicted from the three different test temperatures. The simulations were solved only past the point of initial load drop due to instabilities in the implicit solver related to the presence of element death and deletion. Note that Fig. 16.15 is meant to be demonstrate generally the modeled trends. As mesh convergence is not valid for methods involving element death and deletion, the predicted peak loads should not be considered quantitatively.

As shown in the above figure, the trend towards an increasing fracture toughness with increasing levels of residual stress is correctly captured. To better understand the formation of this trend, the out-of-plane shear and normal strains along the length of the plane-strain model's adhesive layer were probed for each of the test temperatures after cooling and before the application of the mechanical load (Fig. 16.16). Note that these strains were chosen to best represent the tangential (mode II) and normal (mode I) deformations within the bondline elements, which would aid in understanding the effect of mode mixity.

As shown in Fig. 16.16, there is a sharp increase in both the shear and normal strains at the crack front as the thermal residual stresses increase. Therefore, it was hypothesized that the large shear strains deform the bondline in such a way as to counteract the mode I, *tensile* loading. When the mechanical loading is applied after the residual stresses are formed, the tangential deformations due to the high shear strains resist the opening of a crack and promote higher failure loads.

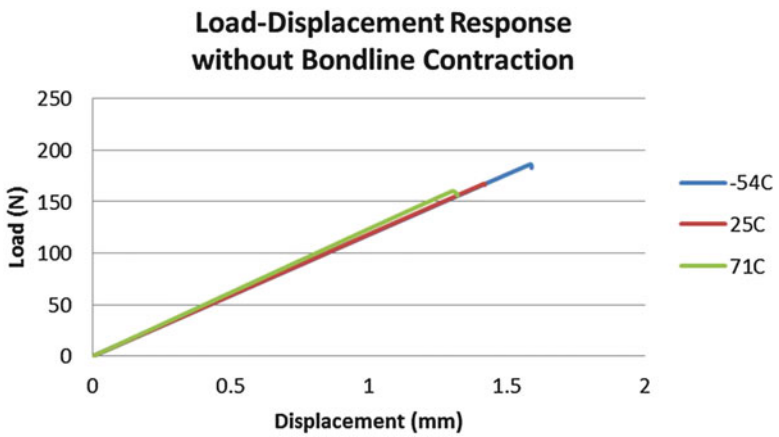

Fig. 16.15 Predicted load-displacement responses with no bondline contraction

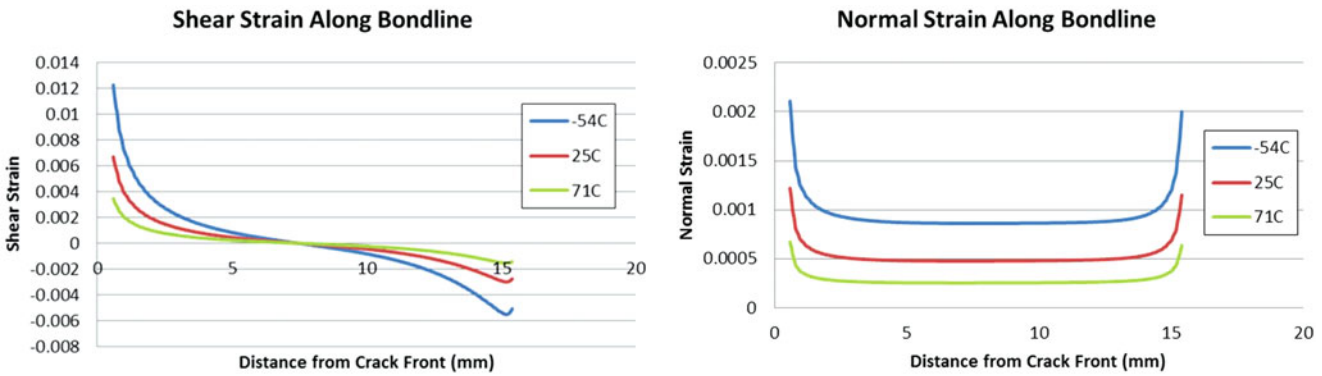

Fig. 16.16 Shear strain (*left*) and normal strain (*right*) along the length of the adhesive layer modeled with no contractions

16.6.2 DCB Simulations with Bondline Contractions

Next, to understand the effect of bondline contractions within the adhesive layer, the simulations described above were repeated with the thermal excursion applied to all model components. The predicted load-displacement responses corresponding to these three simulations are shown in Fig. 16.17.

As shown in Fig. 16.17, the correct trend is again captured, as the predicted peak loads are progressively higher as the residual stress levels increase. Furthermore, when Figs. 16.15 and 16.17 are compared, it is evident that the bondline contractions increase the predicted peak loads slightly. As with the simulations completed with no bondline contractions, the shear and normal strains along the length of the adhesive bondline were examined after the cooling phase of the simulation and, while the shear strains were not affected, the normal strains were significantly decreased (Fig. 16.18).

As shown in Fig. 16.18, it is likely that the thermal contractions of the bondline place the adhesive layer in a state of compression which must be overcome by the mechanical loading, similar to the shear strain effect discussed in the preceding section. Specifically, it is likely that the combined effect of the shear strains formed due to the CTE mismatch of the composite adherends and the compressive strains resulting from the bondline's contraction result is in the higher failure load predictions.

16.6.3 ENF Simulations with Bondline Contractions

The approach taken to modeling the onset of crack growth at various temperatures is similar to that described in the previous section. Prior to element death at the crack tip, the shear stress fields in the bondline are probed approaching the crack tip at each test temperature in both specimen configurations (Fig. 16.19).

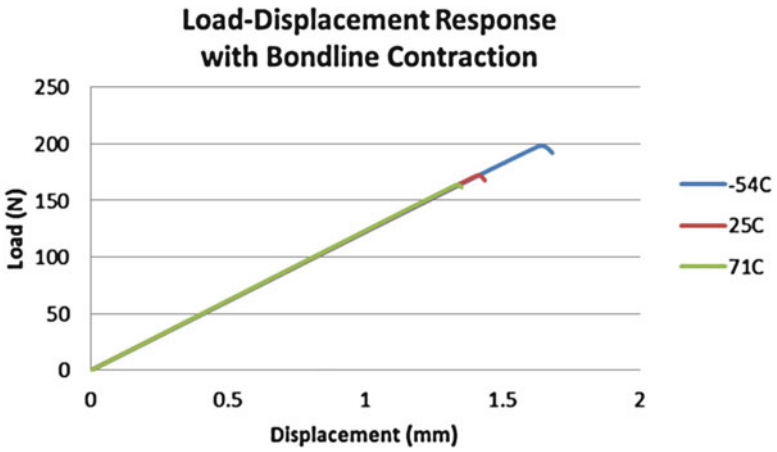

Fig. 16.17 Predicted load-displacement responses including bondline contraction

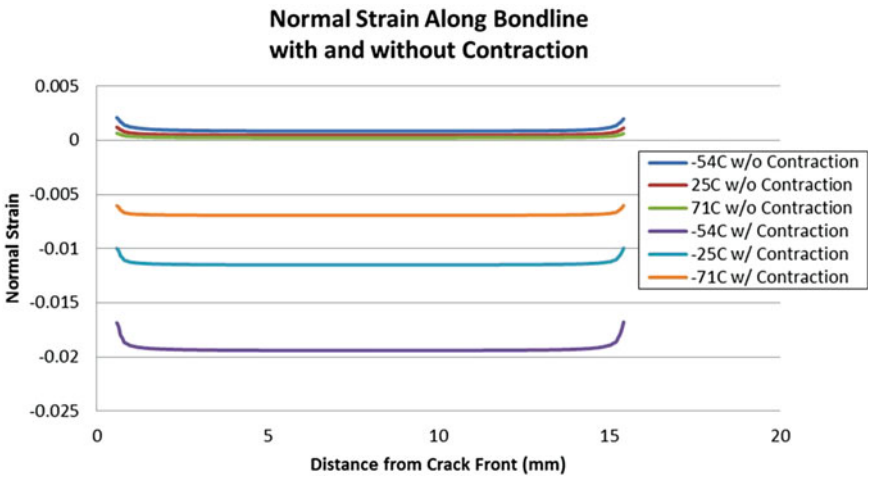

Fig. 16.18 Comparison of the normal strain along the length of the adhesive layer modeled with and without thermal contractions

The trends observed match those of the experiment. When the GFRP is on top, the elevated temperature specimen shows the largest strain value and is closest to failure. However, when the CFRP is on top, the subambient specimen shows the greatest amount of strain. This suggests that the mechanical loading works with the residual strain when the carbon is on top and against it when the glass is on top. Comparison to the experimental results is given in Fig. 16.20.

While the results are heavily mesh dependent, the trend is still accurate. So the failure criteria was tuned to provide good results at room temperature. This resulted in good agreement at elevated temperatures but poor agreement at subambient temperature. This is most likely due to the multiple delaminations seen at cold temperature. If crack growth was restricted to the interface in question, it would most likely have propagated at a lower load.

16.7 Conclusion

Decoupling residual stresses from fracture properties is very important to providing proper material properties to designers of complex structures. Typical zero volume elements such as cohesive zone elements can have trouble accounting for out-of-plane thermal strains that can impact the stress state within a material. It has been shown that these methods capture an improper trend with regards to the effect of increasing ΔT. This may not be a material property as all of the testing in this study was performed well below the glass transition temperature, T_g, of the resin system in the glassy regime. Polymers are known to have significant temperature dependence on their fracture toughness near T_g. By modeling the bondline with a continuum element and using element death, qualitative results match the experimental results quite well. However, this is not a scalable solution as element death is an approach that is significantly mesh dependent and modeling every bondline in a

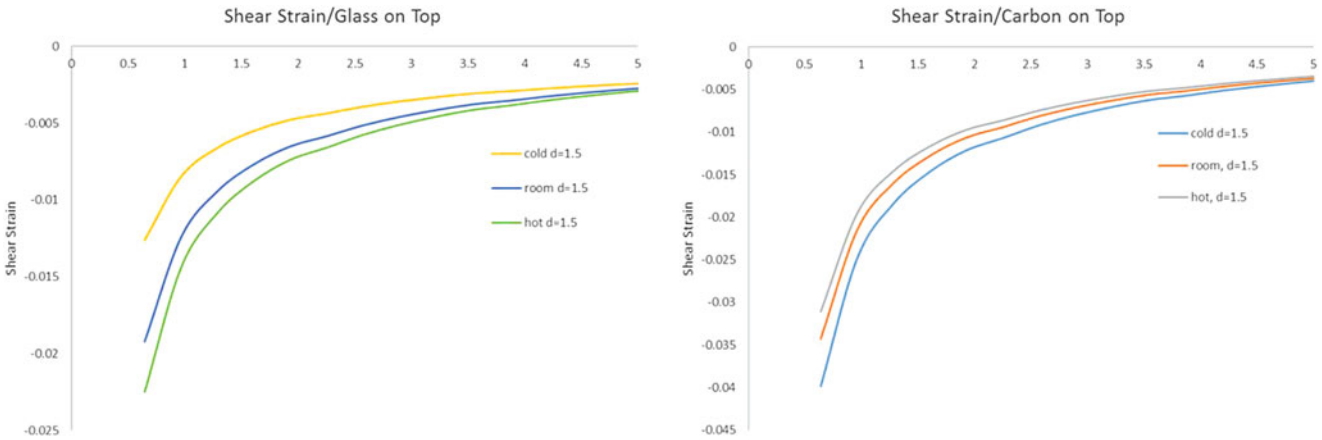

Fig. 16.19 Shear strain profile approaching crack tip for hybrid specimen

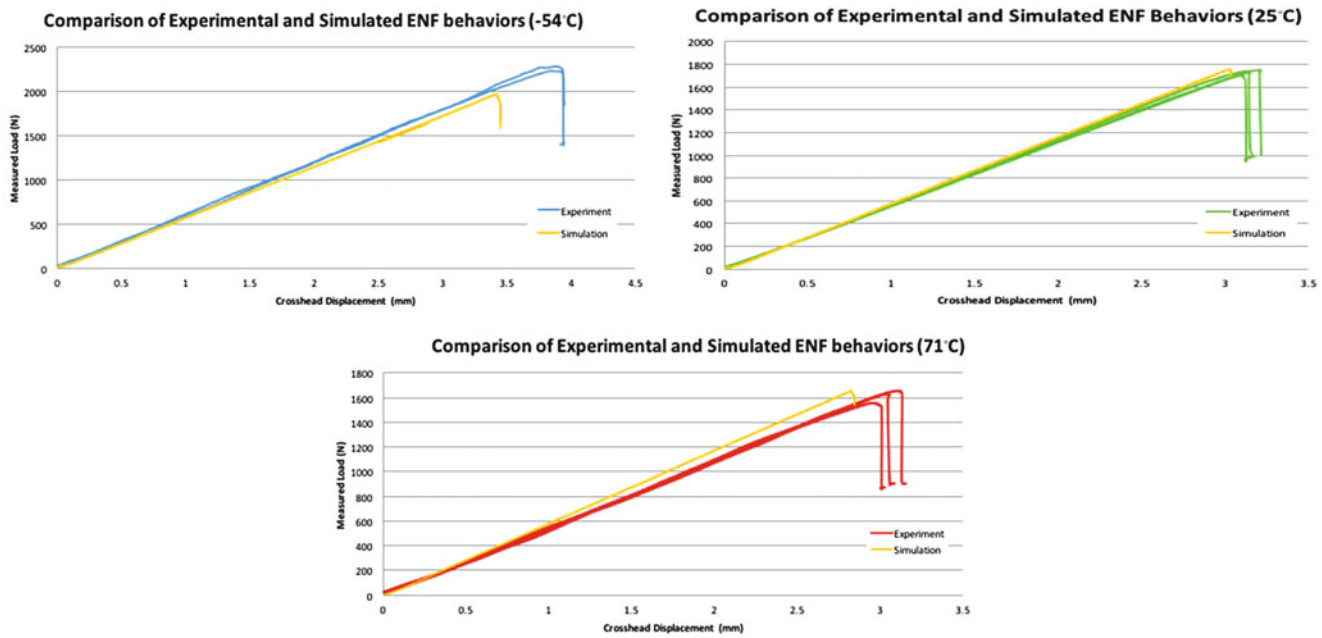

Fig. 16.20 Comparison between experiment and simulated ENF behavior at test temperatures in GFRP on top orientation

laminated structure is not computationally efficient. Further work is needed to characterize whether the residual stress is working to shift the mode-mixity of the stress state at the crack tip from that of the bulk material or if the traction-separation law must be adjusted to account for the residual stress state in the laminate.

Acknowledgement Sandia National Laboratories is a multi-mission laboratory managed and operated by Sandia Corporation, a wholly owned subsidiary of Lockheed Martin Corporation, for the U.S. Department of Energy's National Nuclear Security Administration under contract DE-AC04-94AL85000.

References

1. Camanho, P.P., Davila, C.G., Moura, M.F.D.: Numerical simulation of mixed-mode progressive delamination in composite materials. J. Compos. Mater. **37**(16), 1415–1438 (2003)
2. Li, S., et al.: Mixed-mode cohesive-zone models for fracture of an adhesively bonded polymer–matrix composite. Eng. Fract. Mech. **73**(1), 64–78 (2006)
3. Sun, C.T., Jin, Z.H.: Modeling of composite fracture using cohesive zone and bridging models. Compos. Sci. Technol. **66**(10), 1297–1302 (2006)
4. Yang, Q., Cox, B.: Cohesive models for damage evolution in laminated composites. Int. J. Fract. **133**(2), 107–137 (2005)
5. Nairn, J.A.: Energy release rate analysis for adhesive and laminate double cantilever beam specimens emphasizing the effect of residual stresses. Int. J. Adhes. Adhes. **20**(1), 59–70 (2000)
6. Yokozeki, T., Ogasawara, T., Aoki, T.: Correction method for evaluation of interfacial fracture toughness of DCB, ENF and MMB specimens with residual thermal stresses. Compos. Sci. Technol. **68**(3–4), 760–767 (2008)
7. Warnock, C., Briggs, T.: Cure Cycle Development and Qualification for Thick Section Composites. SAMPE, Long Beach (2016)
8. International, A: Standard Test Method for Mode I Interlaminar Fracture Toughness of Unidirectional Fiber-Reinforced Polymer Matrix Composites. ASTM International, West Conshohocken (2013)
9. Brown, A.A., et al.: Modeling Interfacial Fracture in Sierra. Sandia National Laboratories, Livermore (2013)
10. ASTM: Standard Test Method for Determination of the Mode II Interlaminar Fracture Toughness of Unidirectional Fiber-Reinforced Polymer Matrix Composites. ASTM International, West Conshohocken (2014)
11. Carlsson, L.A., Gillespie, J.W., Pipes, R.B.: On the analysis and design of the End Notched Flexure (ENF) specimen for mode II testing. J. Compos. Mater. **20**(6), 594–604 (1986)
12. Fenner, J.S.: Damage Tolerance Enhancement of Carbon Fiber Reinforced Polymer Composites by Nanoreinforcement of Matrix, in Theoretical and Applied Mechanics. Northwestern University, Evanston (2014)
13. SIERRA SolidMechanics Team: SIERRA/SolidMechanics 4.38 User's Guide. Sandia National Laboratories, Albuquerque (2015)
14. Velmurugan, R., Gurusideswar, S.: Strain rate dependent behavior of glass/nano clay filled epoxy resin composite. Def. Sci. J. **64**(3), 295–302 (2014)
15. Gurusideswar, S., Velmurugan, R., Gupta, N.K.: High strain rate sensitivity of epoxy/clay nanocomposites using non-contact strain measurement. Polymer. **86**, 197–207 (2016)
16. Mallick, P.: Fiber-Reinforced Composites: Materials, Manufacturing, and Design. Marcel Dekker, Inc, New York (1993)
17. Hanson, A., et al.: Experimental measurement and finite element analysis of residual stresses in simple composite structures. CAMX 2016, Anaheim (2016)
18. Nelson, S., Werner, B.: Experimental and computational investigations into the effect of process induced stresses on the mode I fracture toughness of composite materials. CAMX 2016, Anaheim (2016)